Seventh International Conference on Computational Fluid Dynamics (ICCFD7), Big Island, Hawaii, July 9-13, 2012 **ICCFD7-4104**

High-Fidelity Flapping-Wing Aerodynamics Simulations with a Dynamic Grid Spectral Difference Method

Meilin Yu*, Z. J. Wang* and Hui Hu*
Corresponding author: zjw@iastate.edu
* Iowa State University, Ames, IA 50011

Abstract: A dynamic unstructured grid based high-order spectral difference (SD) method is developed to solve the three dimensional compressible Navier-Stokes (N-S) equations. The capability of the developed solver in handling complex vortex-dominated flow is demonstrated via the simulations of the three dimensional flapping-wing problems at low Reynolds and Mach numbers. The flow fields around flapping wings of different planforms, namely the rectangular and bio-inspired types, with different kinematics are investigated. The formation of a two-jet-like wake pattern after the flapping wing is explained by analyzing the interaction between wake and wing tip vortex structures. Moreover, based on the aerodynamic force results, it is found that the combined plunging and pitching motion can significantly enhance the flapping wing propulsive performance.

Keywords: Spectral Difference, Navier-Stokes Equations, Flapping-Wing Aerodynamics, Vortex Dominated Flow.

1 Introduction

High-order computational fluid dynamics (CFD) methods (order of accuracy ≥ 3) have attracted a surge of research activities in recent years due to their efficiency and accuracy for problems involving complex physics and geometry, such as aero-acoustic wave propagation and vortex dominated flow. A review of the recent developments of unstructured grid based high-order methods for the Euler and Navier-Stokes (N-S) equations can be found in [1]. As reported by many researchers, algorithm robustness and efficiency, and the effectiveness in resolving discontinuous solutions are major issues that must be resolved before the high order methods are widely adopted in the CFD community.

The spectral difference (SD) method [2] is an unstructured grid based high-order method for solving hyperbolic conservation laws. Its precursor is the conservative staggered-grid Chebyshev multi-domain method [3]. The general formulation of the SD method was first described in [2] for the simplex element. It is then extended to two dimensional (2D) Euler [4] and N-S equations [5, 6]. After that, the SD method was implemented for three dimensional (3D) N-S equations on unstructured hexahedral grids [7]. Later, a weak instability in the original SD method was found independently by Van den Adeele *et al*. [8] and Huynh [9]. Huynh [9] further found that the use of Legendre-Gauss quadrature points as flux points resulted in a stable SD method. This was later proved by Jameson [10] for the one dimensional linear advection equation under an energy stable framework. In Ref. [11], the

SD method was extended to handle the deformable dynamic grid and its ability to cope with complex vortex dominated bio-inspired flow was demonstrated as well. A parallel development of the dynamic unstructured grid based SD method was reported in [12, 13, 14].

As aforementioned, high-order CFD methods are more accurate and efficient for vortex-dominated flow simulations than the traditional second order methods, which are too dissipative to resolve the complex vortex structures. Therefore there is a trend in the CFD community to develop high-order viscous flow solvers to resolve vortex dominated bio-inspired flow recently. Visbal *et al*. [15, 16] have successfully utilized a high-order compact method to simulate the flow field around a SD7003 airfoil. Persson *et al*. [17] have developed a dynamic unstructured grid based discontinuous Galerkin (DG) method for a finite-span wing simulation and compared the results with other numerical methods. Liang *et al*. [12] have successfully used a 2D SD method for a plunging NACA0012 airfoil simulation. Several applications for 2D and 3D SD method in the bio-inspired flow have been reported by Yu *et al*. [11, 18, 19] . Their results demonstrated the effectiveness of the dynamic unstructured grid based SD method for some challenging bio-inspired flow simulations. Ou *et al*. [20] recently developed a 3D SD solver for the finite-span flapping wing simulations. Results from the paper confirmed the potential of using high order methods as an efficient tool for the full scale flapping wing aerodynamics studies. The present paper will summarize the development of the dynamic unstructured grid based SD method and its application for high-fidelity simulations of 3D flapping wings.

The remainder of the paper is organized as follows. In the next section, the dynamic SD method on unstructured hexahedral mesh is introduced. The geometric conservation law during the time-dependent coordinate transformation is then specified and the grid deformation strategy is given as well. The 3D flapping wing cases simulated are stated in Section 3. In Section 4, 2D steady flow test results at low Mach number are firstly presented. Then comparisons between the numerical results for the 3D flapping wing and the experimental results are shown. After these verification cases, numerical results of rectangular and bio-inspired flapping wings with different kinematics are displayed and discussed. Section 5 briefly concludes the paper.

2 Numerical Methods

2.1 Governing Equations

We consider the unsteady compressible N-S equations in conservation form in the physical domain (t, x, y, z)

$$\frac{\partial Q}{\partial t} + \frac{\partial F}{\partial x} + \frac{\partial G}{\partial y} + \frac{\partial H}{\partial z} = 0. \tag{1}$$

Herein, $Q = (\rho, \rho u, \rho v, \rho w, E)^T$ are the conservative variables, where ρ is the fluid density, u, v and w are the Cartesian velocity components, and E is the total initial energy. *F, G, H* are the total fluxes including both the inviscid and viscous flux vectors, i.e., $F = F^i - F^v$, $G = G^i - G^v$ and $H = H^i - H^v$, which take the following forms,

$$F^i = \begin{Bmatrix} \rho u \\ p + \rho u^2 \\ \rho uv \\ \rho uw \\ u(E+p) \end{Bmatrix},\ G^i = \begin{Bmatrix} \rho v \\ \rho uv \\ p + \rho v^2 \\ \rho vw \\ v(E+p) \end{Bmatrix}, H^i = \begin{Bmatrix} \rho w \\ \rho uw \\ \rho vw \\ p + \rho w^2 \\ w(E+p) \end{Bmatrix}, \tag{2}$$

$$F^v = \begin{Bmatrix} 0 \\ \tau_{xx} \\ \tau_{yx} \\ \tau_{zx} \\ u\tau_{xx} + v\tau_{yx} + w\tau_{zx} + \frac{\mu C_p}{Pr} T_x \end{Bmatrix}, \ G^v = \begin{Bmatrix} 0 \\ \tau_{xy} \\ \tau_{yy} \\ \tau_{zy} \\ u\tau_{xy} + v\tau_{yy} + w\tau_{zy} + \frac{\mu C_p}{Pr} T_y \end{Bmatrix},$$

$$H^v = \begin{Bmatrix} 0 \\ \tau_{xz} \\ \tau_{yz} \\ \tau_{zz} \\ u\tau_{xz} + v\tau_{yz} + w\tau_{zz} + \frac{\mu C_p}{Pr} T_z \end{Bmatrix}.$$

In Eq. (2), p is the pressure, μ is dynamic viscosity, C_p is the specific heat at constant pressure, Pr is the Prandtl number, and T is the temperature. The viscous stress tensors for Newtonian fluids are expressed as follows.

$$\begin{aligned} &\tau_{xx} = 2\mu\left(u_x - \frac{u_x + v_y + w_z}{3}\right), && \tau_{yy} = 2\mu\left(v_y - \frac{u_x + v_y + w_z}{3}\right), \\ &\tau_{zz} = 2\mu\left(w_z - \frac{u_x + v_y + w_z}{3}\right), && \tau_{xy} = \tau_{yx} = \mu\left(v_x + u_y\right), \\ &\tau_{xz} = \tau_{zx} = \mu(w_x + u_z), && \tau_{yz} = \tau_{zy} = \mu\left(w_y + v_z\right) \end{aligned} \tag{3}$$

On assuming that the perfect gas law is obeyed, the pressure is related to the total initial energy by $E = \frac{p}{\gamma - 1} + \frac{1}{2}\rho(u^2 + v^2)$ with the constant heat capacity ratio γ, which closes the solution system.

To achieve an efficient implementation, a time-dependent coordinate transformation from the physical domain (t, x, y, z) to the computational domain (τ, ξ, η, ζ), as shown in Fig. 1(a), is applied to Eq. (1). And we obtain

$$\frac{\partial \tilde{Q}}{\partial \tau} + \frac{\partial \tilde{F}}{\partial \xi} + \frac{\partial \tilde{G}}{\partial \eta} + \frac{\partial \tilde{H}}{\partial \zeta} = 0, \tag{4}$$

where

$$\begin{cases} \tilde{Q} = |J|Q \\ \tilde{F} = |J|\left(Q\xi_\tau + F\xi_x + G\xi_y + H\xi_z\right) \\ \tilde{G} = |J|\left(Q\eta_\tau + F\eta_x + G\eta_y + H\eta_z\right) \\ \tilde{H} = |J|\left(Q\zeta_\tau + F\zeta_x + G\zeta_y + H\zeta_z\right) \end{cases}. \tag{5}$$

Herein, $\tau = t$, and $(\xi, \eta, \zeta) \in [-1,1]^3$, are the local coordinates in the computational domain. In the transformation shown above, the Jacobian matrix J takes the following form

$$J = \frac{\partial(x, y, z, t)}{\partial(\xi, \eta, \zeta, \tau)} = \begin{pmatrix} x_\xi & x_\eta & x_\zeta & x_\tau \\ y_\xi & y_\eta & y_\zeta & y_\tau \\ z_\xi & z_\eta & z_\zeta & z_\tau \\ 0 & 0 & 0 & 1 \end{pmatrix}. \tag{6}$$

Note that all the information concerning grid velocity $\overrightarrow{v_g} = (x_t, y_t, z_t)$ is related with $(\xi_\tau, \eta_\tau, \zeta_\tau)$ by

$$\begin{cases} \xi_\tau = -\overrightarrow{v_g} \cdot \nabla\xi \\ \eta_\tau = -\overrightarrow{v_g} \cdot \nabla\eta \\ \zeta_\tau = -\overrightarrow{v_g} \cdot \nabla\zeta \end{cases}. \tag{7}$$

2.2 Geometric Conservation Law

In deriving the strong-conservation form of the N-S equations in the computational domain, the following metrics identities are implicitly invoked,

$$\begin{cases} \dfrac{\partial}{\partial\xi}(|J|\xi_x) + \dfrac{\partial}{\partial\eta}(|J|\eta_x) + \dfrac{\partial}{\partial\zeta}(|J|\zeta_x) = 0 \\ \dfrac{\partial}{\partial\xi}(|J|\xi_y) + \dfrac{\partial}{\partial\eta}(|J|\eta_y) + \dfrac{\partial}{\partial\zeta}(|J|\zeta_y) = 0 \\ \dfrac{\partial}{\partial\xi}(|J|\xi_z) + \dfrac{\partial}{\partial\eta}(|J|\eta_z) + \dfrac{\partial}{\partial\zeta}(|J|\zeta_z) = 0 \\ \dfrac{\partial|J|}{\partial\tau} + \dfrac{\partial}{\partial\xi}(|J|\xi_\tau) + \dfrac{\partial}{\partial\eta}(|J|\eta_\tau) + \dfrac{\partial}{\partial\zeta}(|J|\zeta_\tau) = 0 \end{cases}. \tag{8}$$

An important criterion in the development of the dynamic grid based algorithm is that the physical flow field should not be contaminated by the metrics of the time-dependent transformation. In other words, the developed numerical algorithm must preserve the free stream solutions. It turns out that the first three identities in Eq. (8) can be preserved well if the high-order space discretization is used. However, the last identity in Eq. (8) invokes the time evolution of Jacobian $|J|$ with the grid velocity $\overrightarrow{v_g}$, and careful attentions are needed to ensure the consistency between the Jacobian change and the grid velocity. The last identity is referred to as the geometric conservation law (GCL) by Thomas and Lombard [21]. Two types of methods have been developed to enforce the GCL for high-order schemes. The first approach is to directly correct the GCL errors by balancing the time derivative of Jacobian $|J|$ and the divergence of the grid velocity related flux $(|J|\xi_\tau, |J|\eta_\tau, |J|\zeta_\tau)$ [22, 11]. More details on the GCL error corrections for the explicit Runge-Kutta scheme and the implicit backward Euler type scheme can be found in [11]. Another approach is to numerically solve Jacobian from the last identity in Eq. (8) by using the same time integration scheme as the flow solver, and then substitute the Jacobian in $\tilde{Q}$ with the newly calculated value [23]. The first approach is adopted in the present study.

2.3 Space Discretization

The SD method is used for the space discretization. In the SD method, two sets of points are given, namely the solution and flux points, as shown in Fig. 1(b) for a 2D quadrilateral element. Unknown solutions or degrees of freedom (DOFs) are defined at the solution points (SPs), and fluxes are calculated on flux points (FPs). In the present study, the solution points are chosen as the Chebyshev-Gauss quadrature points. For a P^{N-1} reconstruction, N solution points are needed in 1D and are specified as

$$\xi_s = -\cos\left(\frac{2s-1}{2N} \cdot \pi\right), s = 1,2,\cdots,N \tag{9}$$

It has been proved in Ref. [10] that the adoption of the Legendre-Gauss quadrature points as the flux points can ensure the stability of the SD method. Therefore, the flux points are selected to be the Legendre-Gauss points with end points as -1 and 1. These points are denoted as $\beta_f, f = 0,1,\cdots,N$.

Two sets of Lagrange polynomials based on the solution points and flux points respectively can be specified as follows.

SPs based Lagrange polynomial:

$$L_{s,i}(\xi) = \prod_{s=1,s\neq i}^{N} \frac{\xi - \xi_s}{\xi_i - \xi_s}, i = 1,2,\cdots,N \tag{10}$$

FPs based Lagrange polynomial:

$$L_{f,i}(\beta) = \prod_{f=0,f\neq i}^{N} \frac{\beta - \beta_f}{\beta_i - \beta_f}, i = 0,1,\cdots,N \tag{11}$$

The reconstruction of the SD method is stated briefly as follows. First of all, the inviscid fluxes are reconstructed. Note that the fluxes related to the grid movement are incorporated into the inviscid fluxes, e.g., $\tilde{F}^i = |J|\left(Q\xi_\tau + F^i\xi_x + G^i\xi_y + H^i\xi_z\right)$. The conservative variables Q_f on the flux points are interpolated from the conservative variables Q_s on the solution points via a tensor production of the 1D Lagrange polynomial Eq. (10), which takes the following form

$$Q_f(\xi,\eta,\zeta) = \sum_{k=1}^{N}\sum_{j=1}^{N}\sum_{i=1}^{N} Q_s\left(\xi_i,\eta_j,\zeta_k\right)L_{s,i}(\xi)L_{s,j}(\eta)L_{s,k}(\zeta). \tag{12}$$

Then the fluxes can be reconstructed at the flux points using Q_f. Note that this reconstruction is continuous within a standard element, but discontinuous on the cell interfaces. Therefore, a Riemann flux or common flux needs to be specified on the interface to ensure conservation. Since the flow regime for flapping flight is almost incompressible and the present governing equations are compressible N-S equations, the Riemann solver should retain good performance at low Mach numbers. The AUSM$^+$-up Riemann solver [24] for all speed is implemented for the present simulation and is proved to behave well at low Mach numbers. The procedures to reconstruct the common fluxes from the AUSM$^+$-up Riemann solver are stated as follows.

Denote the face normal of arbitrary interface by $\vec{n}$, then the interface mass flow rate $\dot{m}_{1/2}$ reads

$$\dot{m}_{1/2} = a_{1/2}M_{1/2}\begin{cases}\rho_L & if\ M_{1/2} > 0\\ \rho_R & otherwise\end{cases}, \tag{13}$$

where the subscript '1/2' stands for the interface, a and M are speed of sound and Mach number respectively. Note that the grid velocity has been included in the interface Mach number M. The numerical normal fluxes $\tilde{F}^i$, $\tilde{G}^i$ and $\tilde{H}^i$ can then be specified as

$$\begin{cases}\tilde{F}^i = \left(\dot{m}_{1/2}\begin{cases}\psi_L & if\ \dot{m}_{1/2} > 0\\ \psi_R & otherwise\end{cases} + P_{1/2}\right)|J||\nabla\xi|sign(\vec{n}\cdot\nabla\xi)\\ \tilde{G}^i = \left(\dot{m}_{1/2}\begin{cases}\psi_L & if\ \dot{m}_{1/2} > 0\\ \psi_R & otherwise\end{cases} + P_{1/2}\right)|J||\nabla\eta|sign(\vec{n}\cdot\nabla\eta),\\ \tilde{H}^i = \left(\dot{m}_{1/2}\begin{cases}\psi_L & if\ \dot{m}_{1/2} > 0\\ \psi_R & otherwise\end{cases} + P_{1/2}\right)|J||\nabla\zeta|sign(\vec{n}\cdot\nabla\zeta)\end{cases} \tag{14}$$

where $\psi = (1,u,v,w,(E+p)/\rho)^T$, $P = \left(0,pn_x,pn_y,pn_z,0\right)^T$, with n_x, n_y and n_z specifying the face normal components in x, y and z direction respectively.

After this, the derivatives of the inviscid fluxes are calculated on the solution points using the following formulas,

$$\frac{\partial\tilde{F}^i}{\partial\xi}(\xi,\eta,\zeta) = \sum_{k=1}^{N}\sum_{j=1}^{N}\sum_{i=0}^{N} \tilde{F}^i\left(\xi_i,\eta_j,\zeta_k\right)L'_{f,i}(\xi)L_{s,j}(\eta)L_{s,k}(\zeta) \tag{15}$$

$$\frac{\partial \tilde{G}^i}{\partial \eta}(\xi,\eta,\zeta) = \sum_{k=1}^{N}\sum_{j=0}^{N}\sum_{i=1}^{N} \tilde{G}^i(\xi_i,\eta_j,\zeta_k) L_{s,i}(\xi) L'_{f,j}(\eta) L_{s,k}(\zeta)$$
$$\frac{\partial \widetilde{H}^i}{\partial \zeta}(\xi,\eta,\zeta) = \sum_{k=0}^{N}\sum_{j=1}^{N}\sum_{i=1}^{N} \widetilde{H}^i(\xi_i,\eta_j,\zeta_k) L_{s,i}(\xi) L_{s,j}(\eta) L'_{f,k}(\zeta)$$

Since the viscous fluxes are functions of both the conservative variables Q and their derivatives ∇Q, slightly more involved reconstruction procedures are needed. In the present study, the approach proposed in [25], also known as 'BR1', is adopted. The implementation of this approach in SD is briefly introduced as follows.

Let $\vec{R} = \nabla Q$, and on transforming this formula from the physical domain to the computational domain, we obtain the three components of $\vec{R}$ in the conservation form as

$$\begin{aligned} R^x &= \frac{1}{|J|}\left(\frac{\partial |J| Q \xi_x}{\partial \xi} + \frac{\partial |J| Q \eta_x}{\partial \eta} + \frac{\partial |J| Q \zeta_x}{\partial \zeta}\right) \\ R^y &= \frac{1}{|J|}\left(\frac{\partial |J| Q \xi_y}{\partial \xi} + \frac{\partial |J| Q \eta_y}{\partial \eta} + \frac{\partial |J| Q \zeta_y}{\partial \zeta}\right). \\ R^z &= \frac{1}{|J|}\left(\frac{\partial |J| Q \xi_z}{\partial \xi} + \frac{\partial |J| Q \eta_z}{\partial \eta} + \frac{\partial |J| Q \zeta_z}{\partial \zeta}\right) \end{aligned} \tag{16}$$

Then using the conservative variables Q_f on the flux points, the derivatives in Eq. (16) on the solution points can be calculated following the procedure as shown in Eq. (15). Note that the common conservative variables Q^{com} on element interfaces are used in the derivative calculation. In BR1, Q^{com} is the average of the left and right solutions on the interface,

$$Q^{com} = \frac{Q^L + Q^R}{2}. \tag{17}$$

After this, the gradient of Q is then interpolated back to flux points following the procedure as shown in Eq. (12) and the viscous fluxes can then be calculated on flux points. Again, the gradient of Q from the aforementioned reconstruction is generally discontinuous on the element interface, and BR1 is used to provide a common gradient ∇Q^{com} on the element interface,

$$\nabla Q^{com} = \frac{\nabla Q^L + \nabla Q^R}{2}. \tag{18}$$

Thus the viscous fluxes $\tilde{F}^v$, $\tilde{G}^v$,and $\widetilde{H}^v$ on flux points are uniquely specified in a local cell, and the flux derivatives on solution points can then be calculated via the approach as shown in Eq. (15).

Once all flux derivatives are available, the DOFs can be updated with either explicit or implicit time integrations.

2.4 Dynamic Grids Strategy

In order to solve problems with moving grids, it is necessary to design a grid moving algorithm. In this study, a blending function approach proposed in Ref. [23] is used to reconstruct the whole physical domain. The fifth-order polynomial blending function reads

$$r_5(s) = 10s^3 - 15s^4 + 6s^5, s \in [0,1] \tag{19}$$

It is obvious that $r'_5(0) = 0$, $r'_5(1) = 0$, which can generate a smooth variation at both end points during the mesh reconstruction. Herein, 's' is a normalized arc length, which reflects the 'distance' between the present node and the moving boundaries. s=0 means that the present node will move with the moving boundary, while s=1 means that the present node will not move. Therefore, for any motion (transition, rotation), the change of the position vector $\vec{P}$ is

$$\Delta\vec{P}_{present} = (1 - r_5)\Delta\vec{P}_{rigid} \tag{20}$$

After these manipulations, a new set of mesh nodes can be calculated based on $\Delta\vec{P}$. It is clear that for systems with complex relative motions, the algebraic algorithm for the grid motion will be hard to design. However, for many cases this method enjoys its remarkable simplicity and efficiency.

3 Problem Statements

Rectangular and bio-inspired flapping wings, as shown in Fig. 2 are studied here. Wing surface grids and streamwise grids on the symmetric plane are also displayed in Fig. 2. The grid deformation strategy is specified as follows. Suppose that all Lagrangian control points on the flapping wing oscillate only on the plane perpendicular to the spanwise axis. The maximum position of the profile in the plane perpendicular to the chordwise axis is set to be a parabola $h = h_0 r^2$ where $r \in [0,1]$ is the distance from the wing root to the Lagrangian control point normalized by the wing span and h_0 is the flapping amplitude of the wingtip. The rigid-body plunging function for one particular position (x_s, y_s, z_s) on the flapping wing is given as follows,

$$x = x_s, z = z_s, y = y_s + h_s \sin(\omega t) \tag{21}$$

where h_s is determined from the aforementioned parabola. Then the blending function Eq. (19) and the motion control function Eq. (20) are used to determine the movement of other grid points. Herein, $\Delta\vec{P}_{rigid}$ is specified as Δy on the surface of the flapping wing.

For the combined pitching and plunging motion, the pitching part is controlled as below

$$\begin{pmatrix} x_{present} - x_c \\ y_{present} - y_c \end{pmatrix} = \begin{pmatrix} \cos(\Delta\alpha) & -\sin(\Delta\alpha) \\ \sin(\Delta\alpha) & -\cos(\Delta\alpha) \end{pmatrix} \begin{pmatrix} x_{former} - x_c \\ y_{former} - y_c \end{pmatrix} \tag{22}$$

with $y_c = h_{c,s}\sin(\omega t)$ and $\alpha = \alpha_0 cos(\omega t + \phi_0)$. According to the optimal thrust generation conditions suggested by Anderson *et al*. [26], ϕ_0 is set as 75°. Herein, $\Delta\vec{P}_{rigid}$ is specified as $(\Delta x, \Delta y)$ on the surface of the flapping wing.

The studied finite-span flapping wings have the same wing span, aspect ratio of the planform (defined as the ratio of the square of the wing span to the planform area, $L_{span}^2/Area$) and the kinematic parameters of the flapping motion. In the present study, the Strouhal number (Str) of the finite-span flapping wings was selected to be well within the optimal range usually used by flying insects and birds and swimming fishes (i.e., 0.2 < Str < 0.4). For all the simulations during the present study, the Mach number of the free stream is set to be 0.05, under which the flow is almost incompressible. The aspect ratios for all wings are set as 2.6772. The Reynolds number (Re) based on the free stream velocity and the averaged chord length (the planform area divided the wing span, $Area/L_{span}$) is 1,200. The reduced frequency (k) of the flapping motion is 3.5, and the Strouhal number (Str) of the wingtip, based on the definition in Ref. [27], is 0.38. All these parameters are from the experimental setup stated in Ref. [28]. The space discretization accuracy for the simulation is of third order, and the time integration is performed with the explicit three stage TVD Runge-Kutta method [29].

4 Results and Discussions

The performance of the developed solver for low Mach number flow is tested at first for a steady inviscid flow over a NACA0012 airfoil at $Ma_\infty = 0.05$ and zero angle of attack (AOA) with a 3rd order accurate scheme and an implicit LU-SGS time integration [30] on a coarse mesh. The residual convergence history, pressure coefficient ($C_p = (p - p_\infty)/(0.5\rho U_\infty^2)$) contour, and the Mach number contour are displayed in Fig. 3 for the AUSM$^+$-UP Riemann solver (Fig. 3 (a)-(c)) and the standard Roe [31] Riemann solver (Fig. 3 (d)-(f)). Although the residual from the Roe solver can converge to machine zero at $Ma_\infty = 0.05$, the pressure field near the wall surface shows fluctuations. The pressure field from the AUSM$^+$-UP Riemann solver displays no fluctuations. Then a steady viscous flow over a NACA0012 airfoil at $Re = 5{,}000$, $Ma_\infty = 0.05$ and zero AOA is simulated with the same scheme on the same mesh. The residual convergence history, pressure coefficient (C_p) contour, and the Mach number contour are displayed in Fig. 4 for the AUSM$^+$-UP Riemann solver (Fig. 4 (a)-(c)) and the standard Roe Riemann solver (Fig. 4 (d)-(f)). As displayed in the figure, the residual for the standard Roe Riemann solver does not converge and the pressure field shows marked fluctuations. Again, AUSM$^+$-UP Riemann solver works well for the low Mach number viscous flow.

Then the solver is tested using the 3D flapping wing problem as aforementioned. Here in order to compare the numerical results with available experimental results [28], only the plunging motion is adopted as the wing kinematics. The comparisons of the instantaneous vorticity distributions from the numerical simulations and those from experimental measurements in the chordwise cross plane at 50%, 75% and 100% wingspan (i.e., wingtip) and the corresponding time-averaged velocity fields are displayed in Fig. 5. It is observed from the vorticity fields that the wake structures at 50% wingspan from the numerical simulations bear a good visual agreement with the experimental results at the same position. However, at 75% wingspan and the wingtip, numerical results exhibit more elaborate small vortices structures than the experimental results. From the corresponding time-averaged velocity fields at all three positions, it is found that the numerical simulations capture the features of the wakes indicated by experimental measurements reasonably well. Note that all contour levels in the numerical simulations are kept the same as those in the experiments.

4.1 Two-Jet-Like Wake Patterns

The wake vortex structures of the plunging rectangular wings from perspective and side views are shown in Fig. 6 (a) and (b) respectively. In these figures, the vortex structures are indicated by the Q-criterion colored with the streamwise velocity. The Q-criterion is a Galilean-invariant vortex criterion, which is defined as follows

$$Q = \frac{1}{2}\left(R_{ij}R_{ij} - S_{ij}S_{ij}\right) = \frac{1}{2}\frac{\partial u_i}{\partial x_j}\frac{\partial u_j}{\partial x_i} \tag{23}$$

where $R_{ij} = \frac{1}{2}(\frac{\partial u_i}{\partial x_j} - \frac{\partial u_j}{\partial x_i})$, is the angular rotation tensor, and $S_{ij} = \frac{1}{2}(\frac{\partial u_i}{\partial x_j} + \frac{\partial u_j}{\partial x_i})$, is the rate-of-strain tensor. Different vortices have been marked out with rectangular windows or solid arrows which indicate the rotation directions. It is clear from the figures that the complex vortex system around the flapping wing can be decomposed into four parts, namely trailing edge vortices (TEVs), leading edge vortices (LEVs) and tip vortices (TVs), and the entangled vortices (EVs) due to the interactions among TEVs, TVs and LEVs. Similar wake phenomena have been reported by Dong *et al*. [31] for free-end finite-span wings except the complex EVs. The two-jet-like wake patterns discovered at 75%

wingspan in the present study are also reported in Ref. [31]. In that paper it is found that the formation of the two-jet-like wake patterns behind the flapping wing is closely related to the existence of tip vortices. But the reasons for the formation process of the bifurcated jet were not thoroughly analyzed. Herein, a detailed observation of the bifurcated jet effects is shown in Fig. 6 (c) for the fixed-root flapping rectangular wing. The figure shows the 3D vorticity fields indicated by the Q-criterion and the spanwise vorticity field at the 75% wingspan. The trajectories of both clockwise (-) and anti-clockwise (+) vortices are also schematically plotted in the figure. Furthermore, the jet bifurcation position is determined by examining the starting point of the two-jet-like wake patterns from the time-averaged velocity fields in Fig. 5(b). It is observed from the figure that the jet bifurcation occurs when TVs intensively interact with the TEVs and many elaborate small vortices appear in this region.

In order to further examine the physics behind this, a combined flapping and pitching motion with pitching leading plunging cycle by 75^o is used to reduce the separation from the leading edge and the wingtip. The combined plunging and pitching motion maintains a two-jet-like wake pattern at 75% wingspan as shown in Fig. 7 for the time-averaged velocity fields and makes the wake vortex structures much clearer as shown in Fig. 8(a). From Fig. 8(b), it is obvious that the upper branch of the bifurcated jet is formed by an anti-clockwise vortex row consisting of TEVs and a clockwise vortex row consisting of TVs, while the lower branch of the bifurcated jet is formed by an anti-clockwise vortex row consisting of TVs and a clockwise vortex row consisting of TEVs. The reasons that TVs can contribute to the spanwise vorticity can be explained as follows. As shown in Fig. 8(b), because of the existence of TVs2, the end part of the TEVs near the wingtip will be dragged gradually from the 'z' direction to the 'y' direction during the flapping stroke, which indicates that certain amount of vorticity in the vertical (y) direction is generated. The induced rotational velocity field is schematically denoted with the blue dashed arrow near the wingtip part of TEVs3 as displayed in Fig. 8(a). This velocity field will bend the bottom end of TVs3 towards TEVs2, and finally TVs3 have a vorticity component in the spanwise (z) direction. It is not hard to examine that this induced vorticity component is negative as denoted with the blue dashed arrow near the bottom part of TVs3 as shown in Fig. 8(a). This explains the formation of the spanwise vorticity contribution from the TVs and further elucidates the formation of the two-jet-like wake patterns. Note that the above explanation will also work for the plunging case aforementioned, although the existence of small vortices in that case makes the two-jet-like wake formation process hard to distinguish. Similar explanations can be applied to the formation of the wake pattern at the wingtip.

4.2 Aerodynamic Performance of Flapping Wings

In this section two sets of factors on the aerodynamic performance are investigated, namely the wing planform and the wing kinematics. First of all, the wing kinematics is fixed as the plunging motion. The flow fields for both the rectangular and bio-inspired wings at four different phases, namely $0^o, 90^o, 180^o$ and 270^o, are displayed in Fig. 9. Herein, the vortex structures are indicated by the Q-criterion colored by the streamwise velocity. It is found that a large amount of elaborate vortex structures are generated around the flapping wings especially in the wingtip region. It can be inferred from this phenomenon that much flapping energy has been wasted if the pure plunging motion is used as the generated small vortices are hard to be efficiently collected to generate thrust. The comparison of thrust coefficient histories for the rectangular and bio-inspired wings with the pure plunging motion is displayed in Fig. 10(a). The contributions from the pressure force and viscous force for the thrust are shown in Figs. 10(b) and 10(c). From Fig. 10(a), it is found that during one flapping cycle the rectangular wing experiences both larger thrust and drag than the bio-inspired wing. On comparing Figs. 10(b) and 10(c) it is clear that the thrust differences mainly come from the contributions from the pressure force. It is also observed that the bio-inspired wing experience less drag from the viscous force. All these aerodynamic performances of the flapping wings are closely related to the flow structures. As can be found from Fig. 9 that at phases 0^{o} and 180^{o} large LEVs appear near the wingtip regions of both wings and at these phases the flapping wings will experience thrust peaks as shown in Figs. 10(a) and (b). Careful examinations of the flow fields indicates that the pressure change on the leading and trailing edges of the flapping wings mainly occurs in the regions near the wingtip, indicating that the thrust generation is dominated by the outer 50% regions of the flapping wings. It is obvious that at these regions flapping wings have larger flapping amplitudes and speeds and can add more energy to the fluid. Moreover, the associated LEVs can be stabilized by the downwash effects of the TVs and can induce a local low pressure region near the leading edge of the flapping wing. This is beneficial for the thrust production at these phases. It is also found that the LEVs around the rectangular wing at phases 0^{o} and 180^{o} are stronger than those around the bio-inspired wing. As stronger LEVs can induce a lower pressure region near the leading edge of the flapping wing, it is reasonable that the rectangular wing generates more thrust than the bio-inspired wing does at the present simulation parameters. The time-averaged thrust coefficients for these two wings as presented in Table 1. From the table, it is clear that the rectangular wing generates larger thrust than the bio-inspired wing, and for both wings, the pressure force dominates the thrust production. Note that thrust coefficient histories for the two wings in Fig. 10(a) both display small-scale unsteady fluctuations. This is due to the rich vortex structures around the flapping wings as shown in Fig. 9.

Note that according to Table 1 the time-averaged thrust coefficients for the pure plunging wings are very small when compared with the wings under the combined plunging and pitching motion. This can be explained as follows. Based on the knowledge that the pressure force dominates the thrust generation, two parameters, namely the effective wing area projection in the streamwise direction and the pressure difference, will determine the output of the thrust during the flapping flight. Since thin wings are adopted in the present study, if the pure plunging motion is used, the wing area projection in the streamwise direction is very small. This is unfavorable to the thrust production. Therefore, it becomes necessary to add certain pitching motion to the plunging motion to enlarge the wing area projection in the streamwise direction. However, the phase lag between the plunging motion and the pitching motion should be carefully designed as this phase lag will affect the adjustment of the effective AOA. If this parameter is not assigned properly, the performance of the wing can even degrade. As aforementioned, the phase lag between the plunging motion and the pitching motion is set to be 75^{o} as suggested by Anderson *et al.* [26]. The time histories of the total thrust coefficient and the component contributed by the pressure force for the rectangular wing under the combined plunging and pitching motion are displayed in Fig. 11. The corresponding vortex structures indicated by the Q-criterion colored by the streamwise velocity around the flapping wing are shown in Fig. 12 at four phases, namely $0^{o}, 90^{o}, 180^{o}$ and 270^{o}. It is concluded that under the combined motion, the flapping wing can generate much larger (about thirty times) thrust than the pure plunging case as shown in Table 1. Moreover, by comparing the flow fields in Figs. 9 and 12, it is clear that because of the effective AOA adjustment due to the pitching motion, the breakdown of vortices under the combined plunging and pitching motion becomes less severe. This indicated that less kinetic energy is dissipated under the combined motion than under the pure plunging motion.

5 Conclusions

A dynamic unstructured grid based high-order SD compressible N-S solver is developed to perform high-fidelity simulations for 3D vortex-dominated flows. The solver works efficiently for the bio-inspired flows at low Reynolds and Mach numbers and can well capture complex vortex structures around the flapping wing. The flow fields around the rectangular and bio-inspired flapping wings with different kinematics are investigated. The formation of a two-jet-like wake pattern after the flapping wing is explained by analyzing the interaction between wake and wingtip vortex structures. It is found that the bent wingtip vortices play a vital role in the two-jet-like wake pattern formation. Furthermore, based on the aerodynamic force results, it is found that the pure plunging motion is not conducive to the propulsive performance. A combined plunging and pitching motion can drastically increase the thrust production.

Reference

[1] Z. J. Wang, "High-order methods for the Euler and Navier Stokes equations on unstructured grids," *Progress in Aerospace Science*, vol. 43, pp. 1-41, 2007.

[2] Y. Liu, M. Vinokur and Z. J. Wang, "Discontinuous spectral difference method for conservation laws on unstructured grids," *J. Comput. Phys.*, vol. 216, pp. 780-801, 2006.

[3] D. A. Kopriva and J. H. Kolias, "A conservative staggered-grid Chebyshev multi-domain method for compressible flows," *J.Comput.Phys.*, vol. 125, no. 1, pp. 244-261, 1996.

[4] Z. J. Wang, Y. Liu, G. May and A. Jameson, "Spectral difference method for unstructured grids II: extension to the Euler equations," *J. Sci. Comput.*, vol. 32, pp. 45-71, 2007.

[5] G. May and A. Jameson, "A spectral difference method for the Euler and Navier–Stokes equations," in *AIAA Paper 2006-304*, 2006.

[6] Z. J. Wang, Y. Sun, C. Liang and Y. Liu, "Extension of the SD method to viscous flow on unstructured grids," in *the 4th international conference on computational fluid dynamics*, Ghent, Belgium, 2006.

[7] Y. Z. Sun, Z. J. Wang and Y. Liu, "High-order multidomain spectral difference method for the Navier-Stokes equations on unstructured hexahedral grids," *Commun. Comput. Phys.*, vol. 2, pp. 310-333, 2006.

[8] K. V. d. Abeele, C. Lacor and Z. J. Wang, "On the stability and accuracy of the spectral difference method," *J.Sci.Comput.*, vol. 37, no. 2, pp. 162-188, 2008.

[9] H. T. Huynh, "A flux reconstruction approach to high-order schemes including discontinuous Galerkin methods," in *AIAA Paper 2007-4079*, 2007.

[10] A. Jameson, "A proof of the stability of the spectral difference method for all orders of accuracy," *J. Sci. Comput.*, vol. 45, pp. 348-358, 2010.

[11] M. L. Yu, Z. J. Wang and H. Hu, "A high-order spectral difference method for unstructured dynamic grids," *Computer & Fluids*, vol. 48, pp. 84-97, 2011.

[12] C. L. Liang, K. Ou, S. Premasuthan, A. Jameson and Z. J. Wang, "High-order accurate simulations of unsteady flow past plunging and pitching airfoils," *Computer & Fluids*, vol. 40, pp. 236-248, 2010.

[13] K. Ou and A. Jameson, "On the temporal and spatial accuracy of spectral difference method on moving deformable grids and the effect of geometric conservation law," in *AIAA Paper 2010-5032*, 2010.

[14] K. Ou, C. L. Liang and A. Jameson, "A high-order spectral difference method for the Navier-Stokes equations on unstructured moving deformable grids," in *AIAA Paper 2010-541*, 2010.

[15] M. R. Visbal, R. E. Gordnier and M. C. Galbraith, "High fidelity simulations of moving and flexible airfoils at low Reynolds number," *Experiments in Fluids*, vol. 46, pp. 903-922, 2009.

[16] M. R. Visbal, "High-fidelity simulation of transitional flows past a plunging airfoil," in *AIAA Paper 2009-391*, 2009.

[17] P. O. Persson, D. J. Willis and J. Peraire, "The numerical simulation of flapping wings at low Reynolds numbers," in *AIAA Paper 2010-72*, 2010.

[18] M. L. Yu, Z. J. Wang and H. Hu, "The effects of wing planforms on the aerodynamic performance of thin finite-span flapping wings," in *AIAA Paper 2012-0757*, 2012.

[19] M. L. Yu, H. Hu and Z. J. Wang, "Experimental and numerical investigations on the asymmetric wake vortex structures around an oscillating airfoil," in *AIAA Paper 2012-0299*, 2012.

[20] K. Ou, P. Castonguay and A. Jameson, "3D flapping wing simulation with high order spectral difference method on deformable mesh," in *AIAA Paper 2011-1316*, 2011.

[21] P. D. Thomas and C. K. Lombard, "Geometric conservation law and its application to flow computations on moving grids," *AIAA J.*, vol. 17, pp. 1030-1037, 1979.

[22] M. R. Visbal and D. V. Gaitonde, "On the use of high-order finite-difference schemes on curvilinear and deforming meshes," *J. comput. Phys.*, vol. 181, pp. 155-185, 2002.

[23] P. O. Persson, J. Peraire and J. Bonet, "Discontinuous Galerkin solution of the Navier-Stokes equations on deformable domains," *Computer Methods in Applied Mechanics and Engineering*, vol. 198, pp. 1585-1595, 2009.

[24] M. S. Liu, "A sequel to AUSM, Part II: AUSM+-up for all speeds," *J. Comput. Phys.*, vol. 214, pp. 137-170, 2006.

[25] F. Bassi and S. Rebay, "A high-order accurate discontinuous finite element method for the numerical solution of the compressible Navier–Stokes equations," *J. Comput. Phys.*, vol. 131, pp. 267-279, 1997.

[26] J. M. Anderson, K. Streitlien, D. S. Barrett and M. S. Triantafyllou, "Oscillating foils of high propulsive efficiency," *J. Fluid Mech.*, vol. 360, pp. 41-72, 1998.

[27] G. K. Taylor, R. L. Nudds and A. L. R. Thomas, "Flying and swimming animals cruise at a Strouhal number tuned for high power efficiency," *Nature*, vol. 425, pp. 707-711, 2003.

[28] H. Hu, L. Clemons and H. Igarashi, "An experimental study of the unsteady vortex structures in the wake of a root-fixed flapping wing," *Experiments in Fluids*, vol. 51, pp. 347-359, 2011.

[29] C. W. Shu, "Total-Variation-Diminishing time discretizations," *SIAM J. Sci. Stat. Comput.*, vol. 9, pp. 1073-1084, 1988.

[30] Y. Z. Sun, Z. J. Wang and Y. Liu, "Efficient implicit non-linear LU-SGS approach for compressible flow computation using high-order spectral difference method," *Commun. Comput. Phys.*, vol. 5, pp. 760-778, 2009.

[31] P. L. Roe, "Approximate Riemann solvers, parameter vectors, and difference schemes," *J. Comput. Phys.*, vol. 43, pp. 357-372, 1981.

[32] H. B. Dong, R. Mittal and F. Najjar, "Wake topology and hydrodynamic performance of low aspect-ratio flapping foils," *J. Fluid Mech.*, vol. 566, pp. 309-343, 2006.

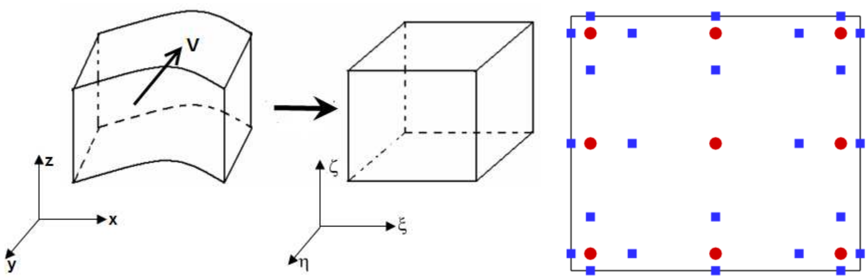

(a) (b)

Fig. 1. (a) Transformation from a moving physical domain to a fixed computational domain; (b) Distribution of solution points (circles) and flux points (squares) in a standard quadrilateral element for a third-order accurate SD scheme.

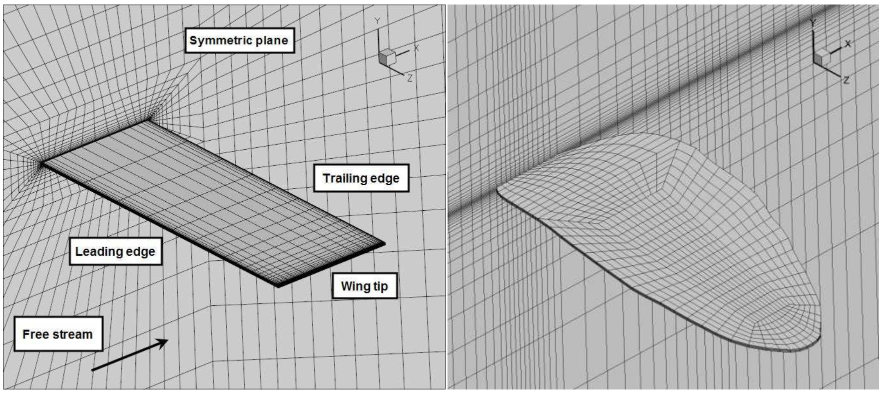

(a) (b)

Fig. 2. Wing surface and root plane meshes for rectangular (a) and bio-inspired (b) wings.

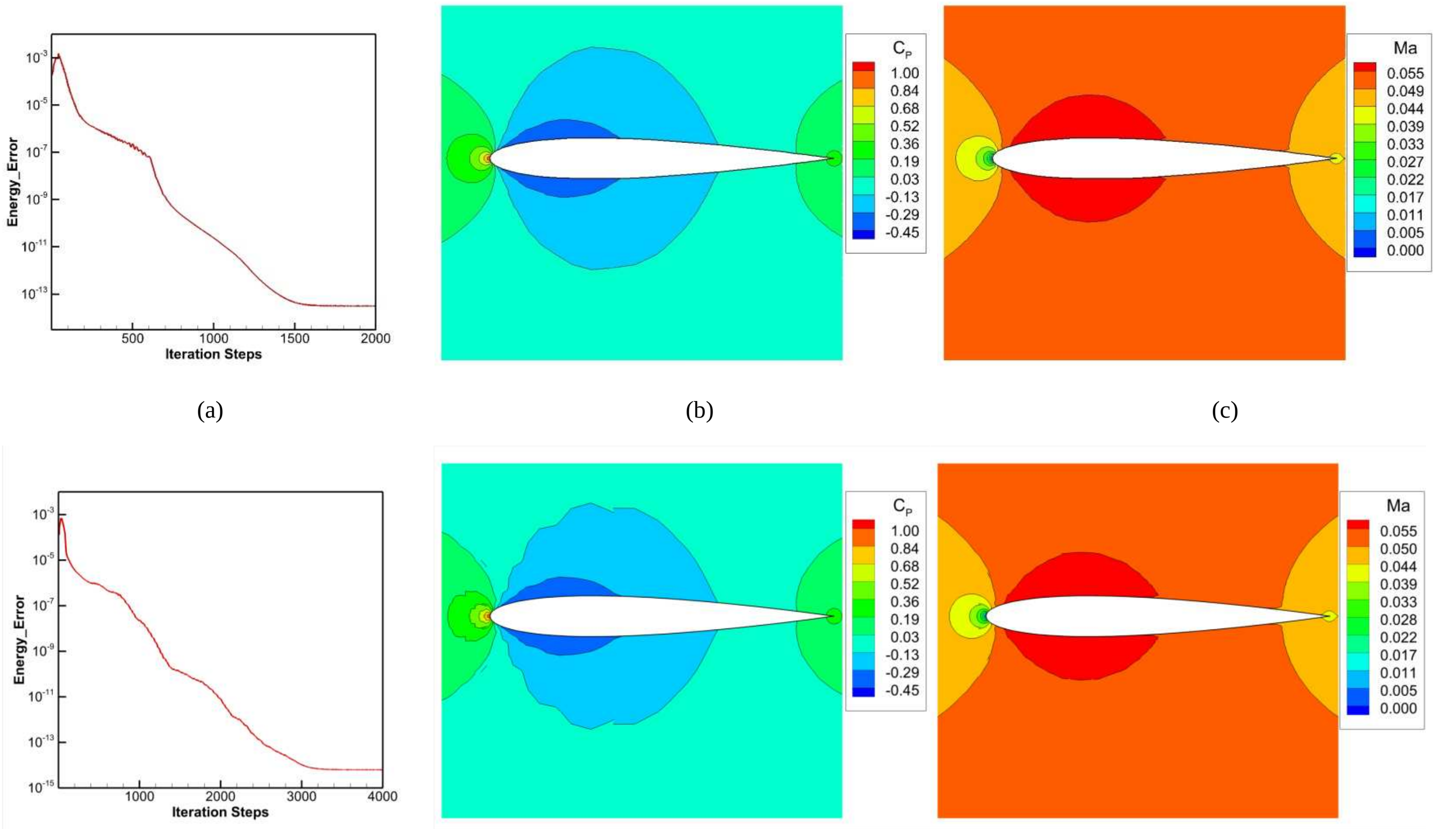

(a) (b) (c)

(d) (e) (f)

Fig. 3. Convergence histories of the energy residual of the steady solution of the inviscid flow over a stationary NACA0012 airfoil with implicit (LU-SGS) time integration at $\mathrm{Ma}_\infty = 0.05$ for the AUSM$^+$-UP Riemann solver (a) and the standard Roe Riemann solver (d); pressure coefficient contours of the converged steady flow for the AUSM$^+$-UP Riemann solver (b) and the standard Roe Riemann solver (e); Mach number contours of the converged steady flow for the AUSM$^+$-UP Riemann solver (c) and the standard Roe Riemann solver (f).

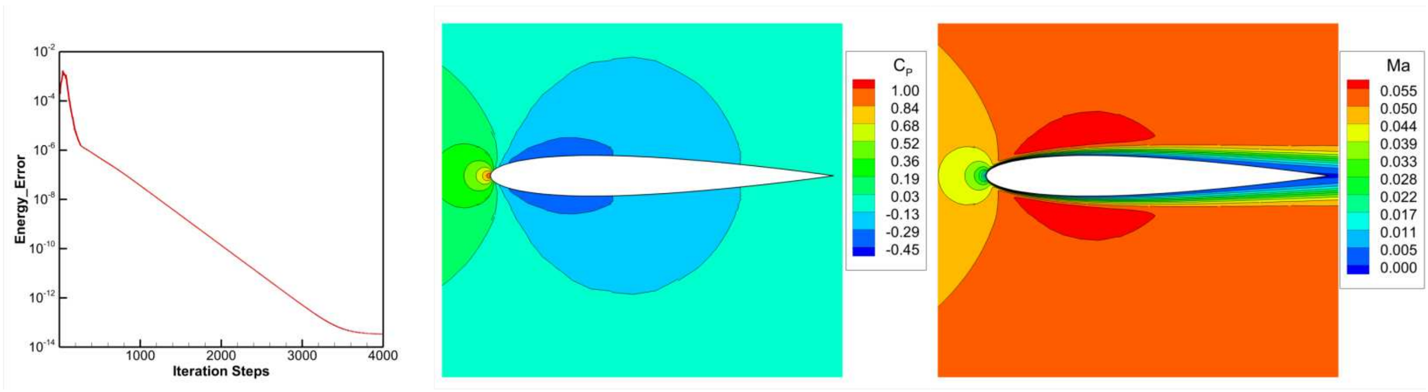

(a) (b) (c)

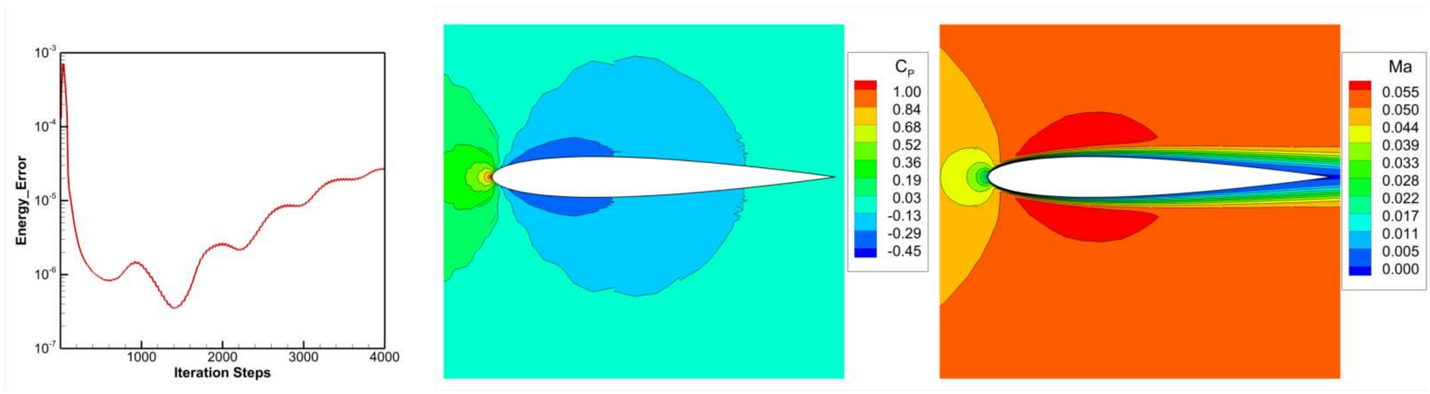

(d) (e) (f)

Fig. 4. Convergence histories of the energy residual of the steady solution of the viscous flow over a stationary NACA0012 airfoil with implicit (LU-SGS) time integration at $\mathrm{Re} = 5{,}000$, $\mathrm{Ma}_\infty = 0.05$ for the AUSM$^+$-UP Riemann solver (a) and the standard Roe Riemann solver (d); pressure coefficient contours of the converged steady flow for the AUSM$^+$-UP Riemann solver (b) and pressure coefficient contours after 4000 iterations for the standard Roe Riemann solver (e); Mach number contours of the converged steady flow for the AUSM$^+$-UP Riemann solver (c) and Mach number contours after 4000 iterations for the standard Roe Riemann solver (f).

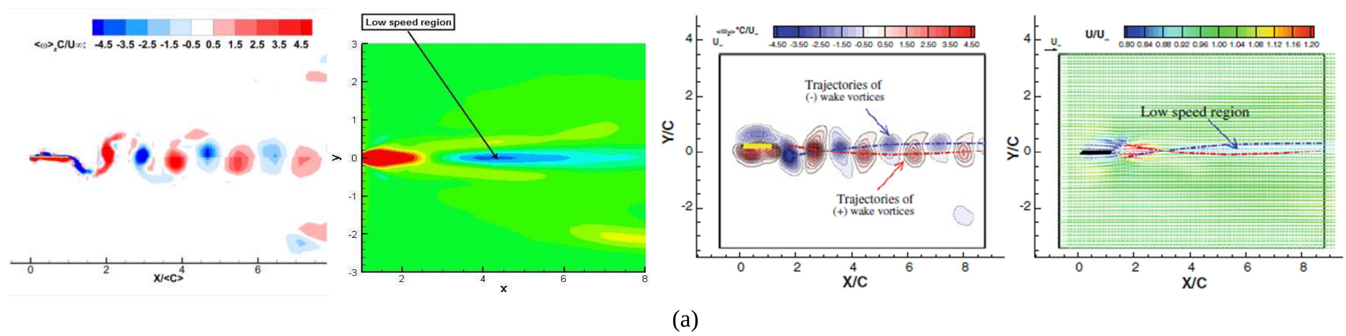

(a)

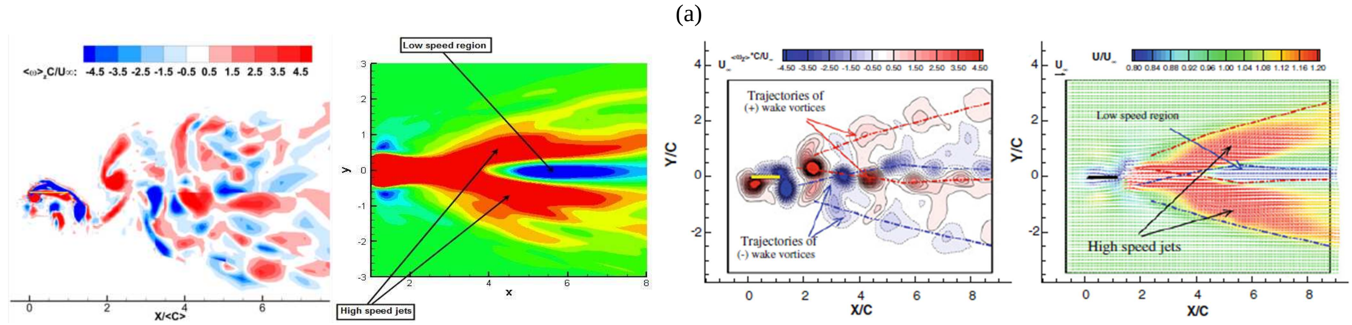

(b)

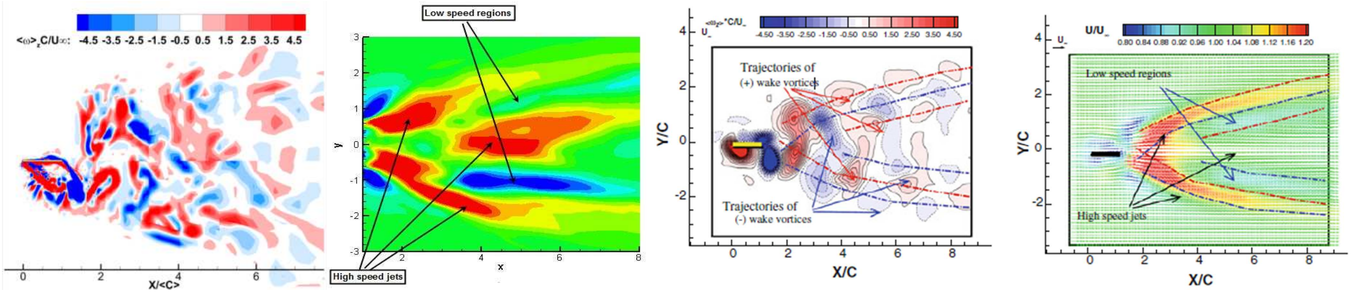

(c)

Fig. 5. Instantaneous vorticity fields and the corresponding time-averaged velocity fields at (a) 50%, (b) 75% wingspan and (c) wingtip for the flapping rectangular wing. Left two columns: numerical results; Right two columns: experimental results (Courtesy of H. Hu, et al. [28]).

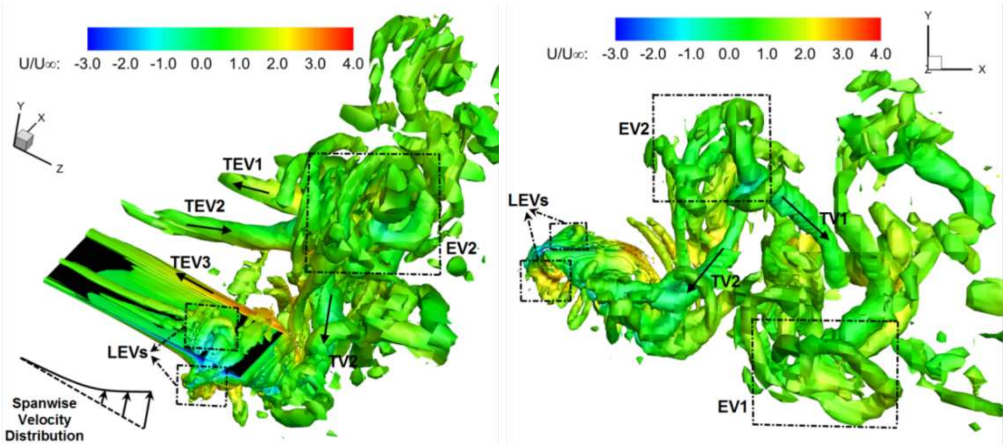

(a) (b)

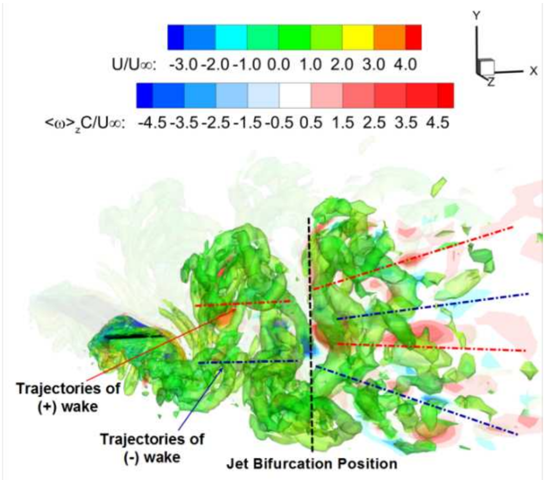

(c)

Fig. 6. Vortex topology around the flapping rectangular wing. Vortex structures are indicated by the Q-criterion and colored by the streamwise velocity. (a) Perspective view. (b) Side view. (c) Perspective view of the vortex structures near the wingtip region and the spanwise vorticity field of the chordwise cross plane at 75% wingspan.

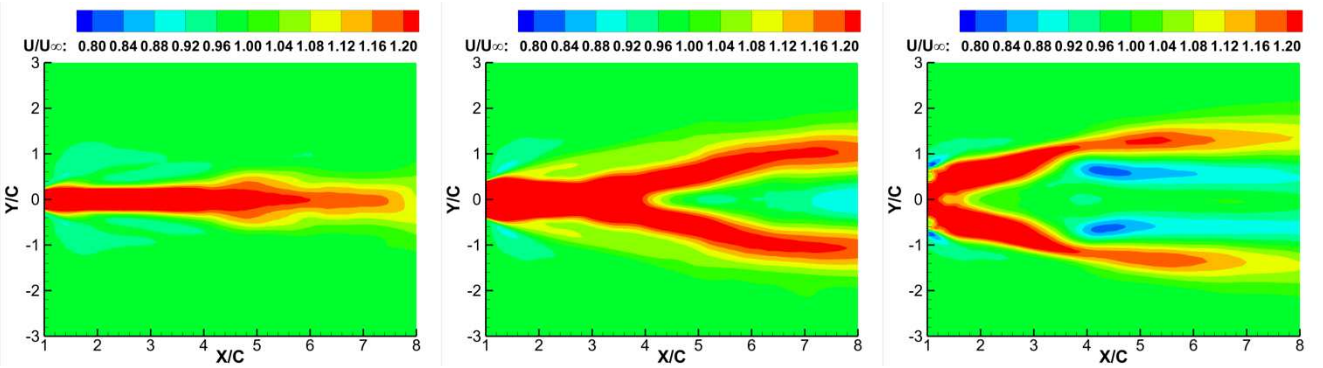

(a) (b) (c)

Fig. 7. Time-averaged velocity fields at (a) 50%, (b) 75% and (c) 100% wingspan for the rectangular wing with a combined plunging and pitching motion.

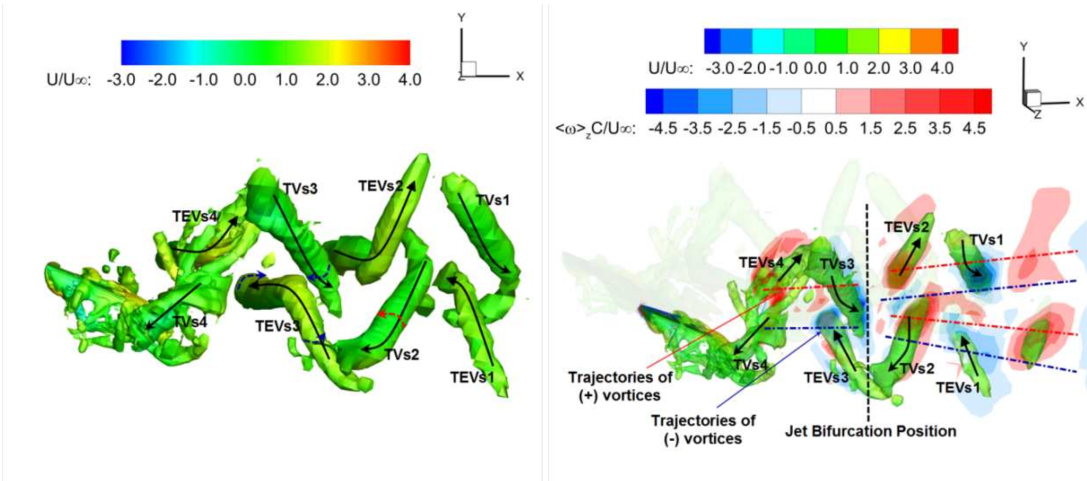

(a) (b)

Fig. 8. Vortex topology around the rectangular wing with a combined plunging and pitching motion. Vortex structures are indicated by the Q-criterion and colored by the streamwise velocity. (a) Side view. (b) Perspective view of the vortex structures near the wingtip region and the spanwise vorticity field of the chordwise cross plane at 75% wingspan.

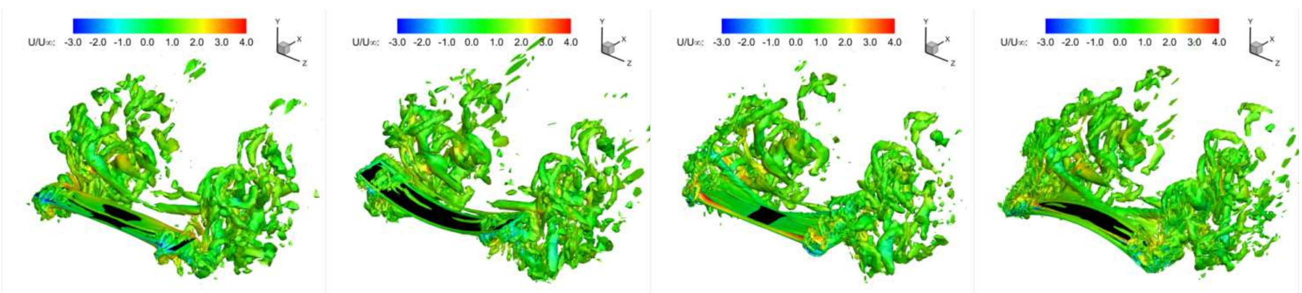

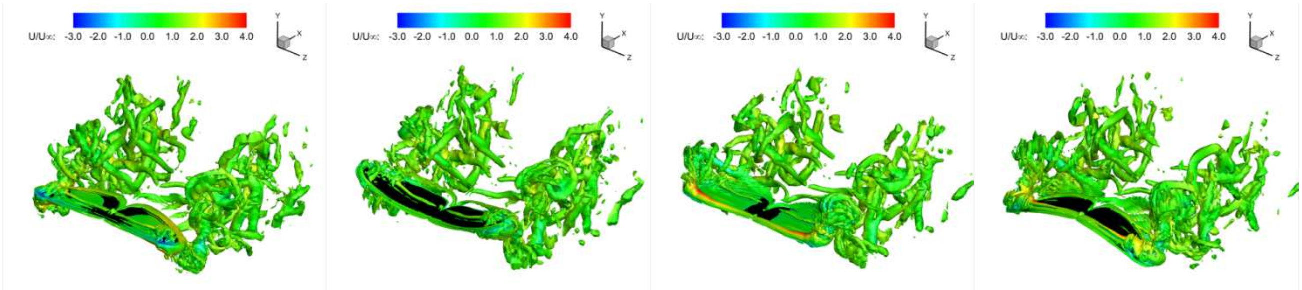

(a) $\phi = 0^o$ (b) $\phi = 90^o$ (c) $\phi = 180^o$ (d) $\phi = 270^o$

Fig. 9. Comparison of the vortex topology for the rectangular and bio-inspired wings at four phases ($0^o, 90^o, 180^o$ and 270^o) with the flapping motion. The upper row is for the rectangular wing; the lower row is for the bio-inspired wing.

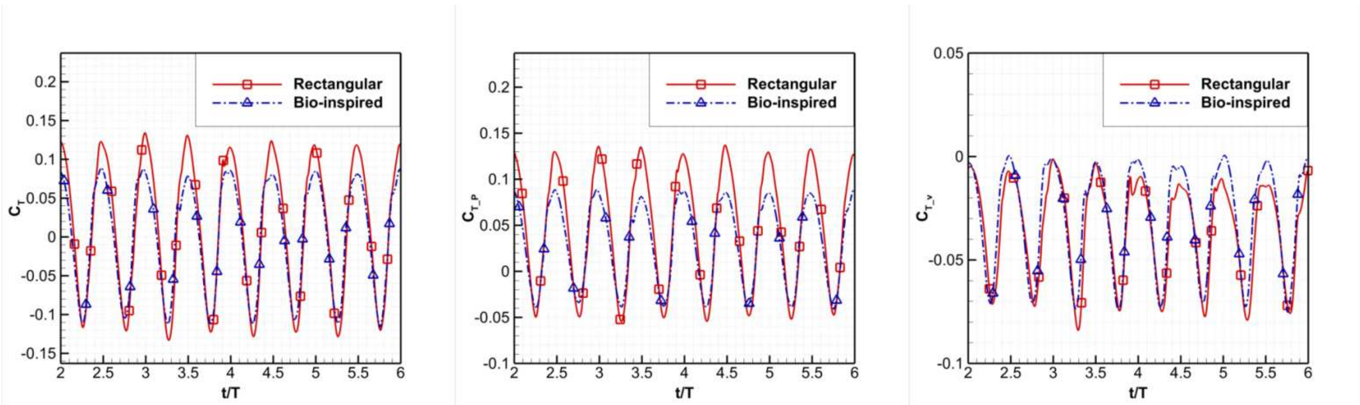

(a) (b) (c)

Fig. 10. The thrust coefficient histories for different wing planforms with the flapping motion. (a) total thrust; (b) contribution from the pressure force; (c) contribution from the viscous force.

	$\bar{C}_T$	$\bar{C}_{T\_P}$	$\bar{C}_{T\_v}$
Rectangular	1.36×10^{-2}	4.72×10^{-2}	-3.36×10^{-2}
Bio-inspired	0.17×10^{-2}	3.07×10^{-2}	-2.90×10^{-2}
Rectangular(Com.)	0.366	0.466	-0.1000

Table 1. Time-averaged thrust coefficient histories for different wing planforms with the flapping motion or the combined motion indicated by 'Com.'. $\bar{C}_T$ stands for the time-averaged total thrust; $\bar{C}_{T\_P}$ stands for the contribution from the pressure force; $\bar{C}_{T\_v}$ stands for the contribution from the viscous force.

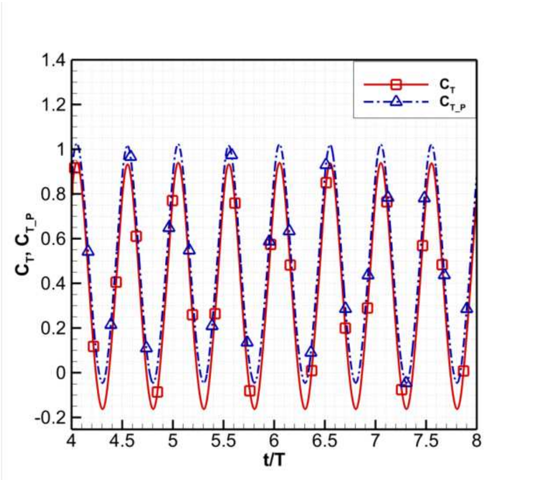

Fig. 11. Time histories of the total thrust coefficient $\mathrm{C_T}$ and pressure-contributed thrust coefficient $\mathrm{C_{T\_P}}$ for the rectangular wing with the combined motion.

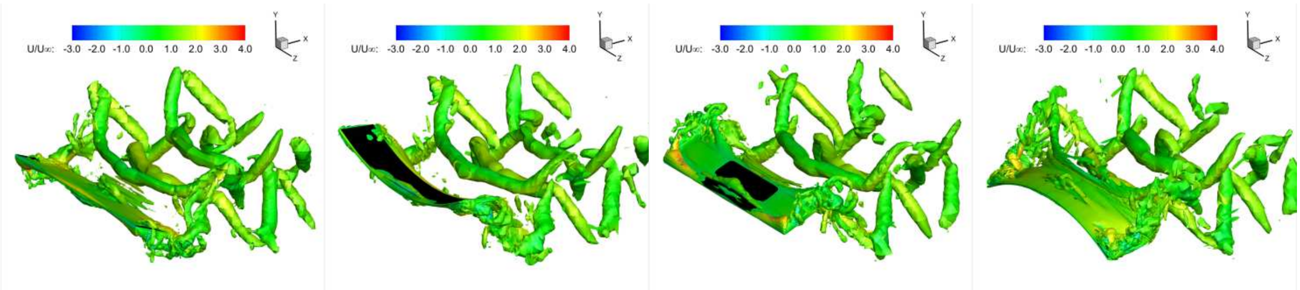

(a) $\phi = 0^o$ (b) $\phi = 90^o$ (c) $\phi = 180^o$ (d) $\phi = 270^o$

Fig. 12. Vortex topology for the rectangular wing at four phases ($0^o, 90^o, 180^o$ and 270^o) with the combined motion.